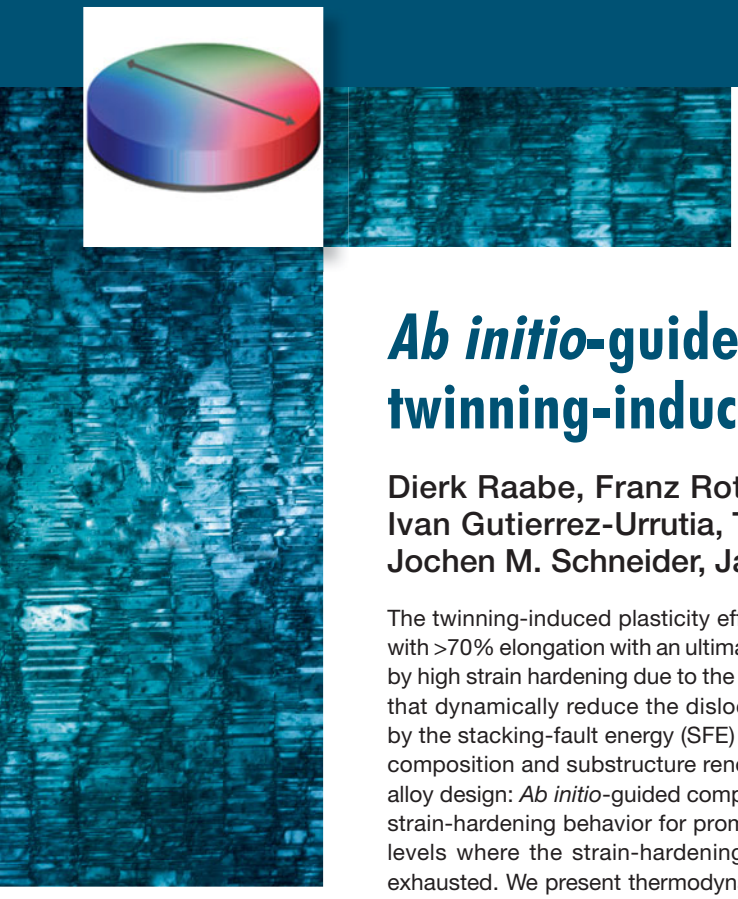

Ab initio-guided design of twinning-induced plasticity steels

Dierk Raabe, Franz Roters, Jörg Neugebauer, Ivan Gutierrez-Urrutia, Tilmann Hickel, Wolfgang Bleck, Jochen M. Schneider, James E. Wittig, and Joachim Mayer

The twinning-induced plasticity effect enables designing austenitic Fe-Mn-C-based steels with >70% elongation with an ultimate tensile strength >1 GPa. These steels are characterized by high strain hardening due to the formation of twins and complex dislocation substructures that dynamically reduce the dislocation mean free path. Both mechanisms are governed by the stacking-fault energy (SFE) that depends on composition. This connection between composition and substructure renders these steels ideal model materials for theory-based alloy design: *Ab initio*-guided composition adjustment is used to tune the SFE, and thus, the strain-hardening behavior for promoting the onset of twinning at intermediate deformation levels where the strain-hardening capacity provided by the dislocation substructure is exhausted. We present thermodynamic simulations and their use in constitutive models, as well as electron microscopy and combinatorial methods that enable validation of the strain-hardening mechanisms.

Introduction

Twins impede dislocation glide. They act as barriers to dislocations, promoting their aggregation and decreasing their mean free path.[1–11] Twinning depends on the stacking-fault energy (SFE).[12–17] In face-centered-cubic (fcc) alloys, the SFE can be tuned by alloying.[18–21] This opens compositional access to "optimal strain-hardening design."[2,11,21–23] This term refers to a state where twins and the associated substructures do not form instantly upon initial yielding, but rather, they form over a wide loading range, so as to enable permanent dynamic reduction of the dislocation free path and hence continuous strain hardening.[8] We can apply this design concept to twinning-induced plasticity (TWIP) steels, as described in this article.

To understand how strain hardening responds to a change in SFE via alloy tuning, the first step lies in identifying its dependence on composition. With this knowledge, the description of the strain-hardening modes can be rendered chemistry sensitive. The next step is to understand the underlying strain-hardening mechanisms. These are twin nucleation and growth, dislocation cross-slip, and twin–slip, slip–slip, and twin–twin interactions.[1,4–8,17]

While the first step is accessible to thermodynamic calculations on the basis of *ab initio*-derived interface energies that can be obtained by density functional theory (DFT) calculations, the second step can be formally rendered by mapping the individual strain-hardening effects into mean field rate equations that are based on internal variables and by coupling the twin nucleation rate to the dislocation substructure and to the SFE. This combination of *ab initio*-derived thermodynamics and constitutive internal variable models renders this alloy design approach into a multiscale plasticity model where *ab initio*-derived quantities are linked with constitutive microstructure evolution equations (**Figure 1**). The constitutive parameters are validated by the measurement of dislocation densities and twin volume fraction fractions using electron channeling contrast imaging (ECCI) and transmission electron microscopy (TEM).[2,8,24] Texture and grain size effects are mapped using electron backscatter diffraction.[18]

Dierk Raabe, Max-Planck-Institut für Eisenforschung, and RWTCH Aachen University, Germany; d.raabe@mpie.de
Franz Roters, Max-Planck-Institut für Eisenforschung, Germany; f.roters@mpie.de
Jörg Neugebauer, Max-Planck-Institut für Eisenforschung, Germany; email neugebauer@mpie.de
Ivan Gutierrez-Urrutia, National Institute for Materials Science, Japan; gutierrezurrutia.ivan@nims.go.jp
Tilmann Hickel, Department of Computational Materials Design, Max-Planck-Institut für Eisenforschung, Germany; t.hickel@mpie.de
Wolfgang Bleck, Steel Institute, RWTH Aachen University, Germany; wolfgang.bleck@iehk.rwth-aachen.de
Jochen M. Schneider, RWTH Aachen University, Germany; schneider@mch.rwth-aachen.de
James E. Wittig, Vanderbilt University, USA; j.wittig@vanderbilt.edu
Joachim Mayer, Central Facility for Electron Microscopy, RWTH Aachen University, and Ernst Ruska-Centre, Forschungszentrum Jülich, Germany; mayer@gfe.rwth-aachen.de
DOI: 10.1557/mrs.2016.63

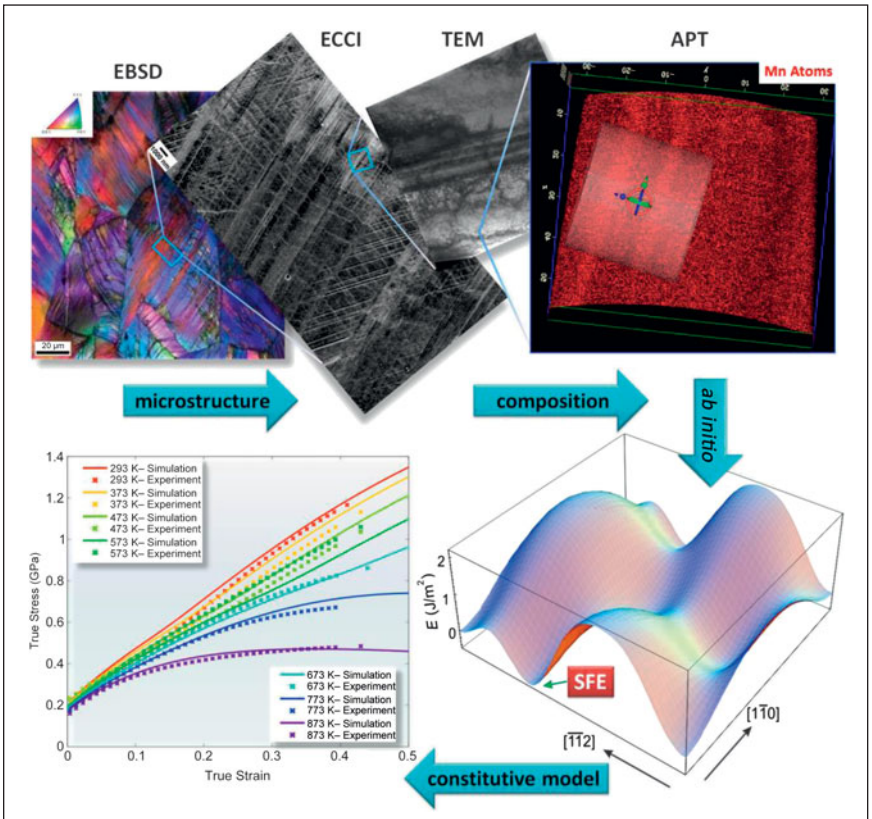

Figure 1. Using *ab initio*-informed internal variable models for describing strain hardening in twinning-induced plasticity (TWIP) steels. The approach considers the composition dependence of the stacking-fault energy (SFE) as a key parameter determining the dynamic refinement of the microstructure as shown in the EBSD, ECCI, TEM, and APT images. The stress–strain curves are for an Fe-22Mn-0.6C TWIP steel (wt%) at different temperatures.[8] Upper row: EBSD texture map revealing twins; ECCI wide field of view image of twins and dislocation arrangements;[2,8] TEM image of the interaction between twins and dislocations; APT map of Mn segregation. Bottom row: ISF energy calculated by *ab initio* methods for one chemical composition. Use of this value in internal variable strain-hardening modeling, including twin nucleation. ECCI, electron channeling contrast imaging; TEM, transmission electron microscope; EBSD, electron backscatter diffraction; APT, atom probe tomography.

Understanding and designing mechanical twinning by *ab initio* modeling

Deformation of TWIP steels can be traced to a few elementary processes on the atomic scale. *Ab initio*-based materials design enables the identification of key control parameters that trigger certain microstructure features, such as twin nucleation (Figure 1).[8] The twin-boundary formation in austenite is characterized by local adaptation of the sequence of {111} atomic layers. Such adaption is only possible if the energy to create the change in the stacking sequence—the SFE—is sufficiently low. Recent advances in *ab initio* simulation tools provide access to the dependence of the SFE on chemical composition, stress state, or temperature with high accuracy.[25,26]

For example, DFT allows for calculation of the SFE dependence on the C content in the Fe-C system. Simulations reveal an enormous increase in SFE with increasing C content.[27] An underlying assumption behind this result is that C atoms are distributed homogenously. This assumption is justified for the undeformed state and would also hold after the formation of stacking faults, provided that C atoms remain trapped at octahedral sites and are displaced together with the lattice during the diffusionless rearrangement. This is realistic, since at room temperature, diffusion of C in fcc Fe is negligible.

To estimate local gradients in the C chemical potential induced by formation of an intrinsic stacking fault (ISF), we performed supercell calculations that contain such a defect.[27] The results reveal there is a significant thermodynamic driving force to out-diffuse C from the local hexagonal close-packed region that is formed next to an ISF. Kinetic simulations indicate that such diffusion will become relevant if the sample is heated by several hundred K[28] (**Figure 2**). Since segregation of solutes out of the defect is opposite to the commonly observed decoration of dislocations (i.e., the Suzuki effect), we refer to it as the anti-Suzuki effect.

Ab initio-based mechanism maps for TWIP steels

For coarse-graining the *ab initio*-calculated SFEs into a wider composition-dependent phase space, a subregular solution thermodynamics model was applied for creating SFE maps for a range of steels.[29,30]

Figure 3 shows three-dimensional (3D) deformation mechanism maps of high-Mn austenitic steels according to the calculation of the SFE, including TRIP (transformation-induced plasticity), TWIP, and MBIP (microband-induced plasticity) effects. A SFE value of 20 mJ/m^2 marks the borderline between TRIP and TWIP,[29–37] and a value of 50 mJ/m^2 is seen as an upper limit for TWIP.[38] With the addition of Al, the SFE increases, and the κ-phase (Fe, Mn)$_3$AlC precipitates in Fe-Mn-Al-C steels.[39–42] Figure 3 reveals the regime where Kappa-carbide occurs (at 873 K) based on CALPHAD (CALculation of PHAse Diagrams) calculations, together with the 3D composition-dependent SFE map of an Fe-Mn-Al-C steel (at 300 K). The SFE maps predict the prevalent deformation mechanisms in Fe-Mn-C and Fe-Mn-Al-C steels; this enables the design of optimal strain hardening.[1,8,9,21,30,43–48]

Combinatorial TWIP steel design

A combinatorial approach was used in translating the simulated trends into real materials. It combined co-sputtering of thin-film composition spreads with high-throughput characterization to define composition–structure–property relationships.[39] Here, we focus on the composition dependence of the elastic properties.

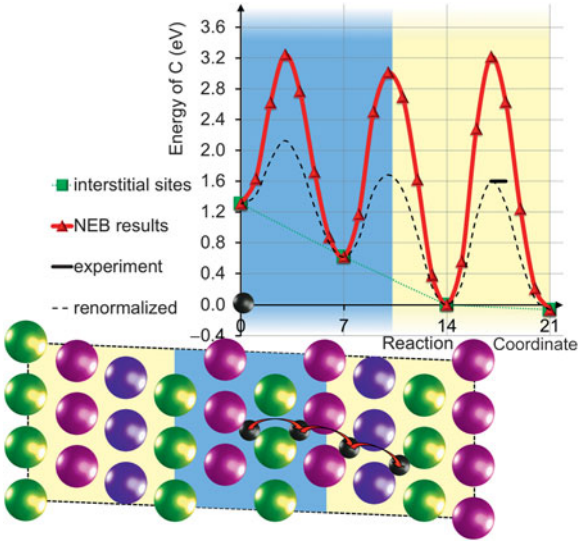

Figure 2. Nonmagnetic *ab initio* calculation of the energetics of a single C atom along a diffusion path from the center of the stacking fault into the matrix. The jump between the (111) atomic layers is schematically shown in the lower part of the figure, where the colors of the atoms indicate the stacking sequence of these layers. The different shaded areas indicate the hexagonal close-packed (center of faults, two kinds of layers) and face-centered-cubic (fcc) stacking sequence (three kinds of layers). The green squared symbols in the upper part of the figure (connected by a dotted line as a guide for the eye) provide the C solution enthalpies in the interstitial sites, whereas the red solid line represents the energy barrier for the diffusion as determined in a nudged-elastic band (NEB) calculation. The black dashed line visualizes an energy profile obtained after renormalizing the *ab initio* values to match the experimental value in the bulk fcc region.[28]

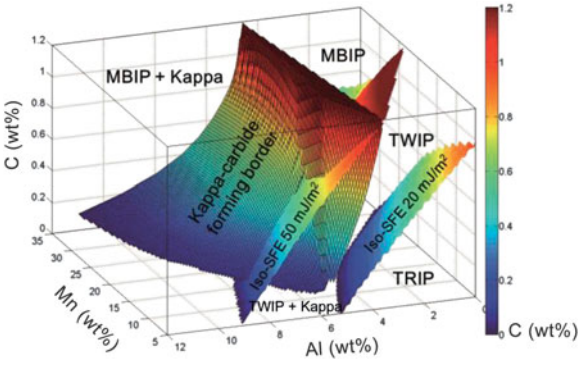

Figure 3. Three-dimensional composition-dependent SFE map for Fe-Mn-Al-C steel at 300 K. Note: MBIP, microband-induced plasticity; TRIP, transformation-induced plasticity; TWIP, twinning-induced plasticity; and SFE, stacking-fault energy.[30]

Figure 4 shows the experimental setup for the co-sputter deposition of Fe-Mn-X composition spreads from Fe-, Mn-, and transition-metal targets (X). Utilizing this experimental setup, Fe-Mn,[49–51] Fe-Mn-C,[52] Fe-Mn-X, X = Al, Si,[53,54] and Fe-Mn-X (X = {Cr, Co, Ni, Cu})[55,56] composition spreads were synthesized.

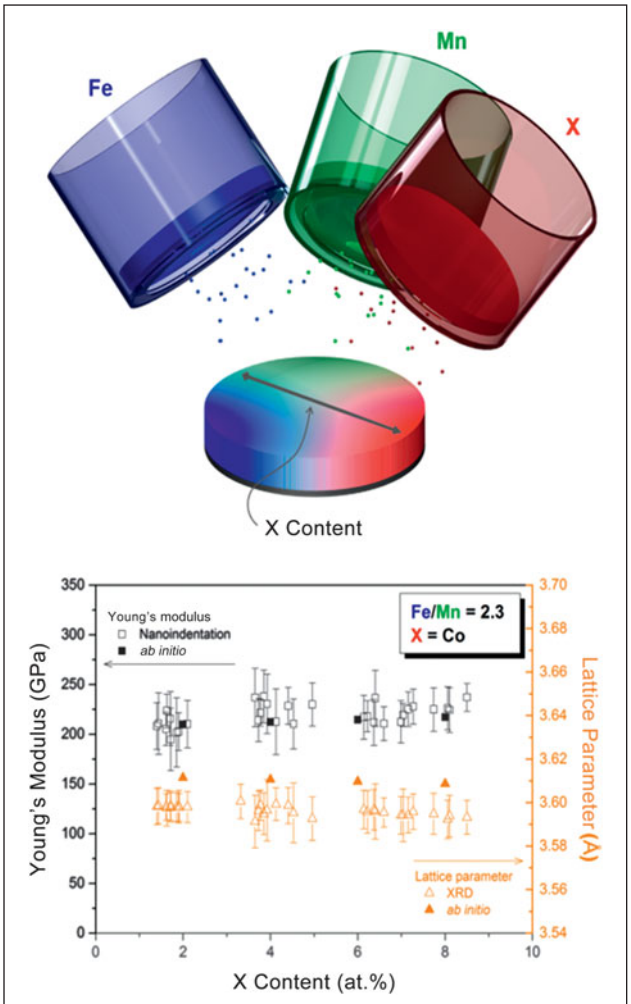

Figure 4. Schematic representation of the combinatorial approach: Fe-Mn-X composition spreads are grown by co-sputtering from three magnetrons where the geometric arrangement of the plasma sources results in concentration gradients. Young's modulus and lattice parameter data obtained by x-ray diffraction (XRD) and nanoindentation experiments along the Co concentration gradient are presented and compared to *ab initio* simulations.[55]

Characterization of the structures by x-ray diffraction and of elastic properties by nanoindentation along the concentration gradients allowed relating the effects of composition on the equilibrium volume and to the Young's modulus. These results were compared to quantum mechanical predictions. This correlative strategy enables validation of structure and elastic properties as well as of the underlying magnetic effects.[50–57] The trends revealed by the thin-film combinatorial results were subsequently used for rapid TWIP alloy screening by a bulk combinatorial approach that included high-throughput synthesis, thermomechanical processing, and mechanical testing of the alloy (i.e., a process sequence referred to as RAP: rapid alloy prototyping).[39] The chemical composition dependence of the Young's modulus data served as input for the plasticity models is described next.[8,58–60]

Constitutive modeling of strain hardening in TWIP steels

The observed dependence of the SFE and the elastic properties on composition were used to inform a constitutive deformation model.[8,58–60] The equations related to the dislocation mechanisms are given in Reference 61. Twinning is split into nucleation and growth. Nucleation is formulated based on the reaction of two dislocations to form a twin nucleus.[4] For the nucleus to grow, a critical stress must be overcome that is dependent on the SFE.[8] The SFE is obtained by combined *ab initio* and thermodynamic modeling.[25–32] Twin growth is instantaneous until an obstacle is encountered. Further details are given in References 8 and 61.

The *ab initio*-informed constitutive model is thus capable of describing the strain-hardening behavior of the TWIP steel as a function of composition (through the SFE), temperature, and strain rate (Figure 1 and **Figure 5**).

TWIP steel microstructures revealed by ECCI

ECCI enables quantitative characterization of the deformation structures of TWIP steels for a wide field of view.[2,8,10,11,62–64] **Figure 6** shows the evolution of the deformation substructure upon tensile deformation in an Fe-22Mn-0.6C (wt%) steel. The orientation dependence of the deformation structures is provided by the TA-IPFs (TA: tensile axis; IPF: inverse pole figure).[18] The ECC image of a dislocation pattern at optimum contrast is characterized by bright structures with a sharp boundary contrast over a dark background. This figure reveals the complex evolution of the dislocation patterns and their interaction with the evolving twin substructure, which is associated with the low SFE of TWIP steels (20–40 mJm^{-2}), high C content, and orientation dependence of the deformation mechanisms.[2,8–11,18,62–64]

At the early stage of deformation (0.1 true strain/380 MPa), the substructure is dominated by dislocation cell blocks (CBs) and dislocation cells (DCs). These patterns are associated with wavy and planar slip characteristics, respectively.[2,18] Crystallographic CBs are formed in grains containing a limited number of {111} active slip systems, such as in grains oriented close to ⟨112⟩//TA directions. Noncrystallographic CBs delimited by high-density dislocation walls (HDDWs) that can deviate by up to 10° from the {111} slip planes are attributed to multiple slips. These dislocation patterns are observed in grains oriented close to ⟨111⟩//TA directions. DCs are built up in grains when a high number of slip planes are activated and dislocation cross-slip is enabled (i.e., grains oriented close to ⟨001⟩//TA directions [red dots in the corresponding TA-IPF shown in Figure 6]).

At higher stress levels (720 MPa), twinning increases, leading to the development of a well-defined twin substructure. At this stage, we can distinguish between three types of deformation substructures, namely, Types I, II, and III. Type I is a twin-free structure that is formed by fine equiaxed DCs. This substructure forms in grains oriented close to ⟨001⟩//TA directions (red dots in the TA-IPF). Type II is characterized by a lamellar twin structure along the primary twinning system. This substructure is formed in grains oriented along the line between ⟨001⟩//TA and ⟨111⟩//TA directions (green dots in the TA-IPF). Type III

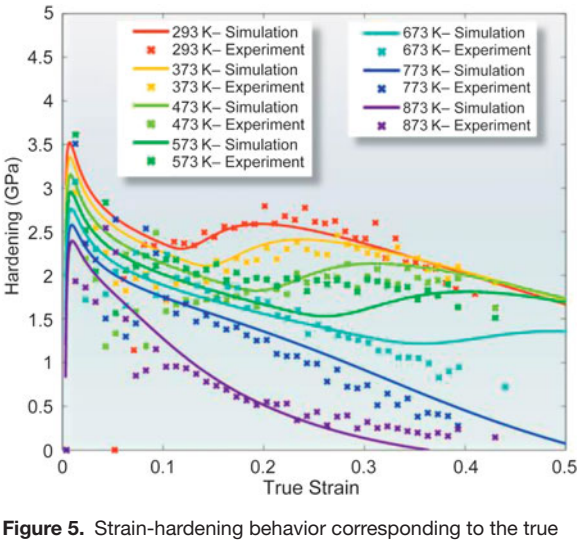

Figure 5. Strain-hardening behavior corresponding to the true stress–true strain curves shown in Figure 1 for an Fe-22Mn-0.6C twinning-induced plasticity steel (wt%) at different temperatures. One parameter set was used for the whole temperature range.[8]

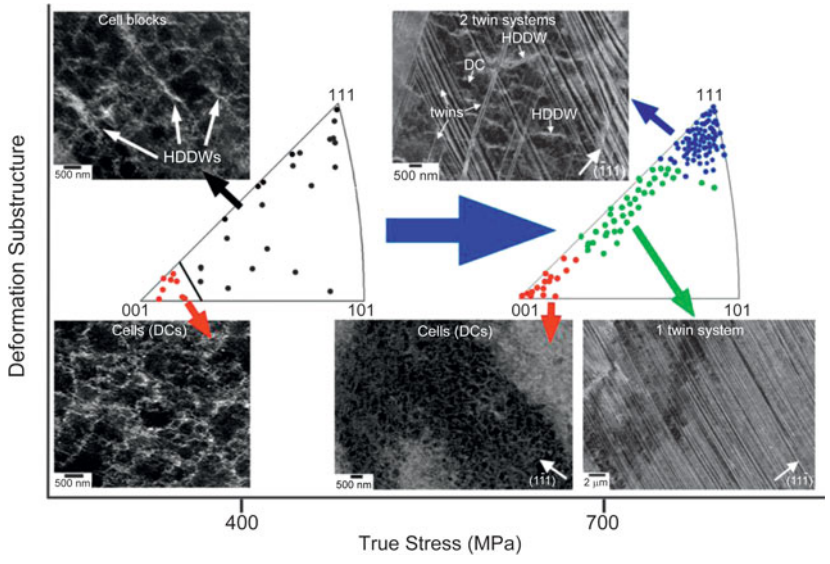

Figure 6. Evolution of the deformation substructure upon tensile deformation in an Fe-22Mn-0.6C (wt%) twinning-induced plasticity steel examined by the electron channeling contrast imaging technique and plotted in tensile axis-inverse pole figure (TA-IPF) diagrams.[2,18] The large blue arrow indicates the texture changes during deformation (HDDW, high-density dislocation wall; DC, dislocation cell).

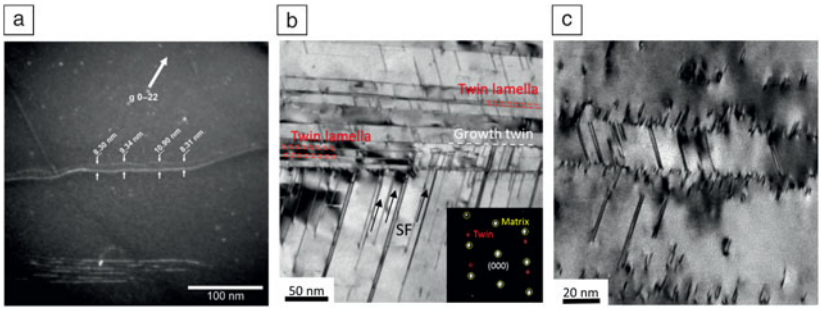

Figure 7. Transmission electron microscope investigations of an austenitic Fe-14Cr-16Mn-0.3C-0.3N alloy. (a) Measurement of Shockley partial-dislocation separation distances based on weak-beam dark-field imaging with a beam direction near [111] on defects in the (111) habit plane using ⟨–220⟩ type g-vectors. The images were acquired using g(3g) diffracting conditions. (b) Bright-field image of extended stacking faults (SFs) blocked at twin lamellae (inset: selected area diffraction pattern) and (c) ⟨111⟩ twin plane reflection showing dislocation pileups at planar defects at a true strain ε = 0.21.[66]

is characterized by a well-defined twin substructure consisting of a primary twin system and one or two secondary twin systems. This substructure forms in crystals oriented close to ⟨111⟩//TA directions (blue dots in the TA-IPF).

TEM-based analysis of the SFE and defect arrangements

Analysis of the influence of SFE on the deformation mechanisms requires an experimental measurement of its value. Analysis of the partial dislocation spacing using weak-beam dark-field (WBDF) TEM techniques[62] has proven adequate for direct SFE determination.[65] A quantitative value of the SFE can be determined from the separation distances of Shockley partial dislocation pairs.[21] **Figure 7**a shows a WBDF image of a partial dislocation pair exhibiting separation distances in the range of 8–10 nm in a sample after light deformation (1.5%). The fitted experimental data indicate a SFE of 21 ± 6 mJ/m^2 for the investigated Fe-14Cr-16Mn-0.3C-0.3N steel.[66]

Further insight into strain hardening can be gained by conventional TEM analysis of strained samples. The primary mechanical twins contribute to the strain hardening by acting as obstacles to dislocations gliding on different slip systems, Figure 7b, which shows mechanical twins and intersecting stacking faults after 0.21 true strain. Dislocation accumulation at the twin boundaries is evident in Figure 7c, which is a higher magnification image of the twinned area in Figure 7a under diffraction conditions that make the dislocation arrangement visible.[66]

Conclusions and outlook

For alloys whose strain hardening is determined by mechanical twinning, *ab initio*-guided alloy design can be realized by revealing the composition dependence of the SFE and by considering these trends in internal variable plasticity models, including twinning, dislocation substructure evolution, and grain-size effects. We applied this concept to the development of Fe-Mn-C-based TWIP steels. Excellent agreement of the predictions was found with combinatorial synthesis and mechanical test data for an Fe-22Mn-0.6C TWIP steel (wt%) between 293 and 873 K using a single set of physically motivated parameters. Applying this design concept in the future and also to other alloy variants in the field of advanced high-strength steels requires including further deformation mechanisms (ε-martensite, α-martensite) and their interdependence. This is specifically important for the development of next-generation middle-Mn high-strength TRIP steels.

Acknowledgments

The authors gratefully acknowledge the financial support of the Deutsche Forschungsgemeinschaft (DFG, German Science Foundation) within the Collaborative Research Center (SFB) 761 "steel–*ab initio*."

References

1. O. Bouaziz, S. Allain, C.P. Scott, P. Cugy, D. Barbier, *Curr. Opin. Solid State Mater. Sci.* **15**, 141 (2011).
2. I. Gutierrez-Urrutia, D. Raabe, *Acta Mater.* **59**, 6449 (2011).
3. O. Bouaziz, N. Guelton, *Mater. Sci. Eng. A* **319**, 246 (2001).
4. H. Karaman, H. Sehitoglu, A.J. Beaudoin, Y.I. Chumlyakov, H.J. Maier, C.N. Tome, *Acta Mater.* **48**, 2031 (2000).
5. F.K. Yan, N.R. Tao, F. Archie, I. Gutierrez-Urrutia, D. Raabe, K. Lu, *Acta Mater.* **81**, 487 (2014).
6. S. Dancette, L. Delannay, K. Renard, M.A. Melchior, P.J. Jacques, *Acta Mater.* **60**, 2135 (2012).
7. R.K.W. Marceau, I. Gutierrez-Urrutia, M. Herbig, K.L. Moore, S. Lozano-Perez, D. Raabe, *Microsc. Microanal.* **19**, 1581 (2013).
8. D.R. Steinmetz, T. Jäpel, B. Wietbrock, P. Eisenlohr, I. Gutierrez-Urrutia, A. Saeed-Akbari, T. Hickel, F. Roters, D. Raabe, *Acta Mater.* **61**, 494 (2013).
9. D. Raabe, H. Springer, I. Gutierrez-Urrutia, F. Roters, M. Bausch, J.-B. Seol, M. Koyama, P.-P. Choi, K. Tsuzaki, *JOM* **66**, 1845 (2014).
10. I. Gutierrez-Urrutia, S. Zaefferer, D. Raabe, *Scr. Mater.* **61**, 737 (2009).
11. I. Gutierrez-Urrutia, D. Raabe, *Acta Mater.* **60**, 5791 (2012).
12. L. Rémy, *Metall. Trans. A* **12**, 387 (1981).
13. J.A. Venables, *Deformation Twinning* (Gordon & Breach, New York, 1964).
14. S. Mahajan, *Philos. Mag.* **23**, 781 (1971).
15. M. Koyama, E. Akiyama, K. Tsuzaki, D. Raabe, *Acta Mater.* **61**, 4607 (2013).
16. J.W. Christian, S. Mahajan, *Prog. Mater. Sci.* **39**, 1 (1995).
17. S. Mahajan, G.Y. Chin, *Acta Metall.* **21**, 1353 (1973).
18. I. Gutierrez-Urrutia, S. Zaefferer, D. Raabe, *Mater. Sci. Eng. A* **527**, 3552 (2010).
19. I. Gutierrez-Urrutia, D. Raabe, *Scr. Mater.* **66**, 992 (2012).
20. L. Rémy, *Acta Metall.* **26**, 443 (1978).
21. D.T. Pierce, J.A. Jimenez, J. Bentley, D. Raabe, C. Oskay, J.E. Wittig, *Acta Mater.* **68**, 238 (2014).
22. I. Gutierrez-Urrutia, R. Marceau, M. Herbig, D. Raabe, *Adv. Mater. Res.* **783–786**, 755 (2014).
23. I. Gutierrez-Urrutia, J.A. Del Valle, S. Zaefferer, D. Raabe, *J. Mater. Sci.* **45**, 6604 (2010).
24. I. Gutierrez-Urrutia, D. Raabe, *Adv. Mater. Res.* **783–786**, 750 (2014).
25. A. Dick, F. Körmann, T. Hickel, J. Neugebauer, *Phys. Rev. B Condens. Matter* **84**, 125101 (2011).
26. T. Hickel, B. Grabowski, F. Körmann, J. Neugebauer, *J. Phys. Condens. Matter* **24**, 053202 (2011).
27. A. Abbasi, A. Dick, T. Hickel, J. Neugebauer, *Acta Mater.* **59**, 3041 (2011).
28. T. Hickel, S. Sandlöbes, R.K.W. Marceau, A. Dick, I. Bleskov, J. Neugebauer, D. Raabe, *Acta Mater.* **75**, 147 (2014).
29. A. Saeed-Akbari, J. Imlau, U. Prahl, W. Bleck, *Metall. Mater. Trans. A* **40A**, 3076 (2009).
30. W. Song, T. Ingendahl, W. Bleck, *Acta Metall. Sin.* **27**, 546 (2014).
31. A.T. Dinsdale, *CALPHAD* **15**, 37 (1991).
32. A. Saeed-Akbari, L. Mosecker, A. Schwedt, W. Bleck, *Metall. Mater. Trans. A* **43A**, 1688 (2012).
33. S. Allain, J.P. Chateau, O. Bouaziz, *Mater. Sci. Eng. A* **387**, 143 (2004).
34. P.H. Adler, G.B. Olsen, W.S. Owen, *Metall. Trans. A* **17A**, 1725 (1986).

35. B.W. Oh, S.J. Cho, Y.G. Kim, Y.P. Kim, W.S. Kim, S.H. Hong, *Mater. Sci. Eng. A* **197**, 147 (1995).
36. S. Allain, J.P. Chateau, D. Dahmoun, O. Bouaziz, *Mater. Sci. Eng. A* **387**, 272 (2004).
37. K. Renard, S. Ryelandt, P.J. Jacques, *Mater. Sci. Eng. A* **527**, 2969 (2010).
38. K.T. Park, G. Kim, K.K. Sung, S.W. Lee, S.W. Hwang, C.S. Lee, *Met. Mater. Int.* **16**, 1 (2010).
39. H. Springer, D. Raabe, *Acta Mater.* **60**, 4950 (2012).
40. J.-B. Seol, D. Raabe, P. Choi, H.-S. Park, J.-H. Kwak, C.-G. Park, *Scr. Mater.* **68**, 348 (2013).
41. I. Gutierrez-Urrutia, D. Raabe, *Scr. Mater.* **68**, 343 (2013).
42. I. Gutierrez-Urrutia, D. Raabe, *Mater. Sci. Technol.* **30**, 1099 (2014).
43. C. Herrera, D. Ponge, D. Raabe, *Acta Mater.* **59**, 4653 (2011).
44. M. Kuzmina, D. Ponge, D. Raabe, *Acta Mater.* **86**, 182 (2015).
45. O. Dmitrieva, D. Ponge, G. Inden, J. Millán, P. Choi, J. Sietsma, D. Raabe, *Acta Mater.* **59**, 364 (2011).
46. D. Raabe, D. Ponge, O. Dmitrieva, B. Sander, *Adv. Eng. Mater.* **11**, 547 (2009).
47. Y.H. Wen, H.B. Peng, D. Raabe, I. Gutierrez-Urrutia, J. Chen, Y.Y. Du, *Nat. Commun.* **5**, 5964 (2014).
48. M. Kuzmina, M. Herbig, D. Ponge, S. Sandlöbes, D. Raabe, *Science* **349**, 1080 (2015).
49. T. Gebhardt, D. Music, T. Takahashi, J.M. Schneider, *Thin Solid Films* **520**, 5491 (2012).
50. D. Music, T. Takahashi, L. Vitos, C. Asker, I.A. Abrikosov, J.M. Schneider, *Appl. Phys. Lett.* **91**, 191904 (2007).
51. T. Gebhardt, D. Music, M. Ekholm, I.A. Abrikosov, J. von Appen, R. Dronskowski, D. Wagner, J. Mayer, J.M. Schneider, *Acta Mater.* **59**, 1493 (2011).
52. S. Reeh, D. Music, T. Gebhardt, M. Kasprzak, T. Jäpel, S. Zaefferer, D. Raabe, S. Richter, A. Schwedt, J. Mayer, B. Wietbrock, G. Hirt, J.M. Schneider, *Acta Mater.* **60**, 6025 (2012).
53. T. Gebhardt, D. Music, M. Ekholm, I.A. Abrikosov, L. Vitos, A. Dick, T. Hickel, J. Neugebauer, J.M. Schneider, *J. Phys. Condens. Matter* **23**, 246003 (2011).
54. T. Gebhardt, D. Music, D. Kossmann, M. Ekholm, I.A. Abrikosov, L. Vitos, J.M. Schneider, *Acta Mater.* **59**, 3145 (2011).
55. S. Reeh, M. Kasprzak, C.D. Klusmann, F. Stalf, D. Music, M. Ekholm, I.A. Abrikosov, J.M. Schneider, *J. Phys. Condens. Matter* **25**, 245401 (2013).
56. S. Reeh, D. Music, M. Ekholm, I.A. Abrikosov, J.M. Schneider, *Phys. Rev. B Condens. Matter* **87**, 224103 (2013).
57. J. Staunton, B.L. Gyorffy, A.J. Pindor, G.M. Stocks, H. Winter, *J. Magn. Magn. Mater.* **45**, 15 (1984).
58. F. Roters, P. Eisenlohr, C. Kords, D.D. Tjahjanto, M. Diehl, D. Raabe, *Procedia IUTAM* **3**, 3 (2012).
59. F. Roters, P. Eisenlohr, L. Hantcherli, D.D. Tjahjanto, T.R. Bieler, D. Raabe, *Acta Mater.* **58**, 1152 (2010).
60. A. Ma, F. Roters, D. Raabe, *Acta Mater.* **54**, 2169 (2006).
61. F. Roters, "Advanced Material Models for the Crystal Plasticity Finite Element Method—Development of a General CPFEM Framework," Habilitation, RWTH Aachen, Germany (2011).
62. I. Gutierrez-Urrutia, S. Zaefferer, D. Raabe, *JOM* **65**, 1229 (2013).
63. S. Zaefferer, N.-N. Elhami, *Acta Mater.* **75**, 20 (2014).
64. I. Gutierrez-Urrutia, D. Raabe, *Scr. Mater.* **69**, 53 (2013).
65. D.B. Williams, C.B. Carter, *Transmission Electron Microscopy: A Text Book for Materials Science*, 2nd ed. (Springer, New York, 2009).
66. L. Mosecker, D.T. Pierce, A. Schwedt, M. Beighmohamadi, J. Mayer, W. Bleck, J.E. Wittig, *Mater. Sci. Eng. A* **642**, 71 (2015). □